Appl. Math. Mech. -Engl. Ed., **43**(12), 1901–1920 (2022)

APPLIED MATHEMATICS AND MECHANICS (ENGLISH EDITION)

https://doi.org/10.1007/s10483-022-2942-7

Three-dimensional interfacial fracture analysis of a one-dimensional hexagonal quasicrystal coating*

Xin ZHANG[1], Minghao ZHAO[1,2], Cuiying FAN[1],
C. S. LU[3], Huayang DANG[1,†]

1. School of Mechanics and Safety Engineering, Zhengzhou University, Zhengzhou 450001, China;
2. School of Mechanical Engineering, Zhengzhou University, Zhengzhou 450001, China;
3. School of Civil and Mechanical Engineering, Curtin University,
Western Australia 6845, Australia

(Received Jun. 5, 2022 / Revised Aug. 22, 2022)

Abstract In this paper, the three-dimensional (3D) interfacial fracture is analyzed in a one-dimensional (1D) hexagonal quasicrystal (QC) coating structure under mechanical loading. A planar interface crack with arbitrary shape is studied by a displacement discontinuity method. Fundamental solutions of interfacial concentrated displacement discontinuities are obtained by the Hankel transform technique, and the corresponding boundary integral-differential equations are constructed with the superposition principle. Green's functions of constant interfacial displacement discontinuities within a rectangular element are derived, and a boundary element method is proposed for numerical simulation. The singularity of stresses near the crack front is investigated, and the stress intensity factors (SIFs) as well as energy release rates (ERRs) are determined. Finally, relevant influencing factors on the fracture behavior are discussed.

Key words one-dimensional (1D) hexagonal quasicrystal (QC) coating, displacement discontinuity method, interface crack, rectangular element, stress intensity factor (SIF), energy release rate (ERR)

Chinese Library Classification O343.1
2010 Mathematics Subject Classification 52C23, 74B05, 78M15

1 Introduction

Quasicrystals (QCs), neither crystalline nor non-crystalline, are a relatively new kind of solid materials with a special arrangement of atoms[1]. Due to their unique microstructure, QCs have high hardness, high temperature resistance, corrosion resistance, and low surface energy[2–4]. However, brittleness of QCs at room temperature makes them difficult to use directly[5]. As a

* Citation: ZHANG, X., ZHAO, M. H., FAN, C. Y., LU, C. S., and DANG, H. Y. Three-dimensional interfacial fracture analysis of a one-dimensional hexagonal quasicrystal coating. *Applied Mathematics and Mechanics* (*English Edition*), **43**(12), 1901–1920 (2022) https://doi.org/10.1007/s10483-022-2942-7

† Corresponding author, E-mail: danghuayang@zzu.edu.cn

Project supported by the National Natural Science Foundation of China (Nos. 11572289, 1171407, 11702252, and 11902293) and the China Postdoctoral Science Foundation (No. 2019M652563)

result, these distinct characteristics endow QCs with great potential as coating materials, such as thermal barrier coatings[6], corrosion-resistant coatings[7], deicing coatings[8–9], and many others[10–11]. It is found that more than 100 kinds of metal alloys have QC phases. Compared with traditional ceramic coatings, QC coatings have a better alloy compatibility and a higher temperature super-plasticity[12]. With these excellent properties, QCs are regarded as an ideal coating candidate in automotive engines devices, aerospace, and solar energy industries[5].

Numerous studies have been done on production of QC coating, where a common process for preparing QC coating is thermal spraying[13–16]. Compared with laser cladding[17] and physical vapor deposition[20], thermal spraying can be applied to deposit a thicker coating on almost any substrate with an extremely low porosity. In order to improve their microstructures and properties, research is mainly focused on the preparation process of QC coatings[19–20], in which defects such as micro-cracks and pores are inevitable at interface[22]. Therefore, it is of great significance to elucidate the fracture behavior of interfacial cracks of QC coating[23]. As a typical composite structure, QC coating structures exhibit complex mechanical characteristics, and their interfacial fracture differs from traditional crystals and non-crystal coatings, which increases the difficulty of analysis.

In recent years, many attempts have been made on the elastic solutions and mechanical properties of QCs. For instance, Fan et al.[24] introduced the linear, nonlinear and dynamic fracture theory of QCs. Sun et al.[25] established a mathematical model to study the nonlocal vibration and buckling of embedded QC layered nanoplates with propagator matrix method. Guo et al.[26] studied the interaction between screw dislocations and elliptical hole in a one-dimensional (1D) hexagonal QC with piezoelectric effect. Based on the modified coupled stress theory, Guo et al.[27] investigated the three-dimensional (3D) bending deformation and vibration response of multilayer two-dimensional (2D) decagonal QC nanoplates by using a propagation matrix method. Gao et al.[28] established a new propagation matrix relationship for the 3D exact electric-elastic analysis of 2D decagonal QC multilayer plates subjected to patch loading. Later on, Gao et al.[29] used a state-space method to analyze the dynamic behavior of a multilayer 2D QC cylindrical shell filled with compressible fluid. Hou et al.[30] derived Green's function solution of 1D hexagonal QC coating under tangential force. Li et al.[31] analyzed the sliding frictional contact of a 1D hexagonal piezoelectric QC coating structure with imperfect interface. Fan et al.[32] suggested a coexistence model for QC and crystal and discussed the interface effect of a QC cubic crystal structure. Recently, Dang et al.[33] and Zhao et al.[34] developed a displacement discontinuity method to study the interfacial fracture behavior of 1D hexagonal and 2D decagonal QC coatings. However, all these relevant works are limited to the 2D cases, which cannot reflect the fracture behavior in line with actual working conditions. Thus, it is necessary to conduct the 3D fracture analysis of QC coating.

The displacement discontinuity method is an indirect boundary element method, which has advantages in dealing with crack problems[35]. In contrast with the traditional finite element method, a crack is discretized as one entity, and thus, it reduces the number of final linear equations to be solved. However, the coefficient matrix is not symmetric, which requires a solution of full rank. As the thickness of a QC coating is thin compared with the substrate, there is a large stress gradient in coating, and the coupling of phonon and phase fields cannot be accurately simulated by a finite element method. In this paper, an extended displacement discontinuity method is proposed to investigate the 3D interfacial fracture of 1D hexagonal QC coatings. Such a method is flexible, which is suitable for complex crack and multi-crack problems.

The paper is organized as follows. The 3D basic equations and general solutions are first listed for a 1D hexagonal QC coating on an isotropic elastic substrate in Section 2. Next, the fundamental solutions of the concentrated interfacial displacement discontinuities are derived in Section 3. Then, Section 4 constructs the boundary integral-differential equations, and Section 5 presents Green's functions for the uniform displacement discontinuities within a rectangular

element. After that, Section 6 analyzes the singularity of stresses, with the expressions for stress intensity factors (SIFs) and energy release rate (ERR). Furthermore, a boundary element method is proposed for numerical calculation in Section 7, and in Section 8, numerical simulations are carried out, and influencing factors are discussed. Finally, main conclusions are drawn in Section 9.

2 Basic equations and general solutions

A 1D hexagonal QC can be assumed as a point group of 6 mm, referred to the Cartesian coordinate with an isotropic periodic plane on the Oxy plane and the z-axis along the quasi-periodic direction, and its constitutive equations are given by

$$\begin{cases} \sigma_{ij} = \dfrac{1}{2}C_{ijkl}(u_{k,l} + u_{l,k}) + R_{ijkl}w_{k,l}, \\ H_{ij} = \dfrac{1}{2}R_{ijkl}(u_{k,l} + u_{l,k}) + K_{ijkl}w_{k,l}, \end{cases} \tag{1}$$

where u_i and w_i are the phonon and phason displacements, respectively, σ_{ij} and H_{ij} are the phonon and phason stresses, respectively , and C_{ijkl}, R_{ijkl}, and K_{ijkl} are the elastic constants in phonon and phason fields, and phonon-phason coupling elastic constants, respectively. The subscript comma denotes partial differentiation with respect to the coordinate, and the repeated indices imply their summation from 1 to 3.

Without body forces, equilibrium equations are expressed as[36]

$$\sigma_{ij,j} = 0, \quad H_{ij,j} = 0. \tag{2}$$

The general solution equations for the 1D hexagonal QC can be expressed by four potential functions[36], that is

$$\begin{cases} u_x = \dfrac{\partial \Psi_0}{\partial y} - \displaystyle\sum_{j=1}^{3} \frac{\partial \Psi_j}{\partial x}, \quad u_y = -\frac{\partial \Psi_0}{\partial x} - \sum_{j=1}^{3} \frac{\partial \Psi_j}{\partial y}, \quad u_z = \sum_{j=1}^{3} \alpha_{1j} \frac{\partial \Psi_j}{\partial z_j}, \\ w_z = \displaystyle\sum_{j=1}^{3} \alpha_{2j} \frac{\partial \Psi_j}{\partial z_j}, \quad \sigma_{zz} = \sum_{j=1}^{3} \gamma_{1j} \frac{\partial^2 \Psi_j}{\partial z_j^2}, \quad H_{zz} = \sum_{j=1}^{3} \gamma_{2j} \frac{\partial^2 \Psi_j}{\partial z_j^2}, \\ \sigma_{zx} = c_{44} s_0 \dfrac{\partial^2 \Psi_0}{\partial y \partial z_0} + \displaystyle\sum_{j=1}^{3} s_j \gamma_{1j} \frac{\partial^2 \Psi_j}{\partial x \partial z_j}, \quad \sigma_{yz} = -c_{44} s_0 \frac{\partial^2 \Psi_0}{\partial x \partial z_0} + + \sum_{j=1}^{3} s_j \gamma_{1j} \frac{\partial^2 \Psi_j}{\partial y \partial z_j}. \end{cases} \tag{3}$$

Here, all the material-related constants are given in Ref. [36]. The harmonic potential functions Ψ_j satisfy

$$\Big(\Delta + \frac{\partial^2}{\partial z_j^2}\Big)\Psi_j = 0, \quad j = 0, 1, 2, 3, \tag{4}$$

where Δ is the Laplacian operator and defined as

$$\Delta = \frac{\partial^2}{\partial x^2} + \frac{\partial^2}{\partial y^2}. \tag{5}$$

For an isotropic elastic crystal, the constitutive and governing equations without body forces are

$$\sigma_{ij} = \mu(u_{i,j} + u_{j,i}) + \lambda \delta_{ij} u_{i,i}, \tag{6a}$$

$$\sigma_{ij,j} = 0, \tag{6b}$$

where μ and λ are, respectively, the shear modulus and Lame constant, and δ_{ij} denotes the Kronecker symbol.

For an isotropic elastic crystal, the general solutions to Eq. (6) are[37]

$$\begin{cases} u_x = \dfrac{1}{2\mu}\Big(-\dfrac{\partial\psi_0}{\partial y}+\dfrac{\partial\psi_1}{\partial x}+z\dfrac{\partial\psi_2}{\partial x}\Big), \quad u_y = \dfrac{1}{2\mu}\Big(\dfrac{\partial\psi_0}{\partial x}+\dfrac{\partial\psi_1}{\partial y}+z\dfrac{\partial\psi_2}{\partial y}\Big), \\ u_z = \dfrac{1}{2\mu}\Big(\dfrac{\partial\psi_1}{\partial z}-(3-4v)\psi_2+z\dfrac{\partial\psi_2}{\partial z}\Big), \quad \sigma_{zz} = \dfrac{\partial^2\psi_1}{\partial z^2}-2(1-v)\dfrac{\partial\psi_2}{\partial z}+z\dfrac{\partial^2\psi_2}{\partial z^2}, \\ \sigma_{zx} = -\dfrac{1}{2}\dfrac{\partial^2\psi_0}{\partial y\partial z}+\dfrac{\partial^2\psi_1}{\partial x\partial z}-(1-2v)\dfrac{\partial\psi_2}{\partial x}+z\dfrac{\partial^2\psi_2}{\partial x\partial z}, \\ \sigma_{yx} = \dfrac{1}{2}\dfrac{\partial^2\psi_0}{\partial x\partial z}+\dfrac{\partial^2\psi_1}{\partial y\partial z}-(1-2v)\dfrac{\partial\psi_2}{\partial y}+z\dfrac{\partial^2\psi_2}{\partial y\partial z}, \end{cases} \tag{7}$$

and the potential functions ψ_j satisfy

$$\Big(\Delta+\frac{\partial^2}{\partial z^2}\Big)\psi_j = 0, \quad j = 0, 1, 2. \tag{8}$$

3 Problem description and fundamental solutions

Let us consider a coating made of a 1D hexagonal QC tightly bonded with an isotropic elastic substrate. Here, the substrate is considered as semi-infinite, with a coating thickness h and an arbitrarily shaped planar crack S lying at the interface. A Cartesian coordinate system $(Oxyz)$ was chosen with the Oxy plane as the periodic plane on the interface and the z-axis along the quasi-periodic direction normal to it, where the upper and lower faces of the crack are respectively denoted as S^+ and S^-. Mechanical tractions, p_x, p_y, and p_z, are applied at infinity, as schematically illustrated in Fig. 1.

3.1 Boundary conditions

In the case of a penny-shaped crack S of radius a at the interface in a coating structure (see Fig. 2), we have

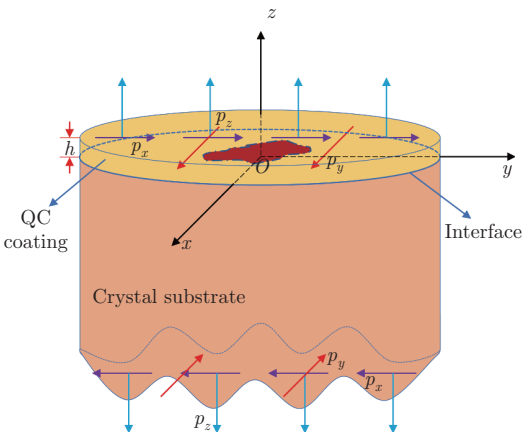

Fig. 1 3D schematic representation of 1D hexagonal QC coating structure with arbitrarily shaped interface crack under mechanical loads (color online)

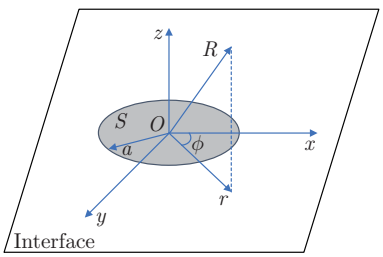

Fig. 2 Illustration of penny-shaped crack with radius of a at interface (color online)

$$\begin{cases} x = r\cos\phi, \\ y = r\sin\phi, \\ R^2 = r^2 + z^2 = x^2 + y^2 + z^2. \end{cases} \tag{9}$$

The displacement discontinuities across crack faces can be expressed as

$$\|u_i\| = u_i(x, y, 0^+) - u_i(x, y, 0^-), \quad i = x, y, z, \quad (x, y) \in S. \tag{10}$$

In accordance with the analogy method[38], when the crack radius a approaches zero, one can obtain the fundamental solutions corresponding to interfacial concentrated displacement discontinuities. These fundamental solutions should satisfy equilibrium equations and the following conditions, namely,

$$\lim_{a\to 0}\int_S \{\|u_x\|, \|u_y\|, \|u_z\|\}\mathrm{d}S = \{1, 0, 0\} \tag{11a}$$

for the concentrated displacement discontinuity in the x-direction,

$$\lim_{a\to 0}\int_S \{\|u_x\|, \|u_y\|, \|u_z\|\}\mathrm{d}S = \{0, 1, 0\} \tag{11b}$$

in the y-direction, and

$$\lim_{a\to 0}\int_S \{\|u_x\|, \|u_y\|, \|u_z\|\}\mathrm{d}S = \{0, 0, 1\} \tag{11c}$$

in the z-direction.

3.2 Fundamental solutions for concentrated $\|\boldsymbol{u_z}\| = \boldsymbol{\delta}$

The boundary condition in Eq. (11c) can be rewritten as an arbitrary interfacial point $(\zeta, \eta, 0)$ within crack faces, and $\delta(\zeta, \eta)$ is the delta function. It is obvious that this is a non-torsional axisymmetric problem about point $(\zeta, \eta, 0)$. According to Fan et al.[32], the phason stress equals zero at the interface, and thus the boundary conditions are

$$u_r^+ = u_r^-, \quad u_z^+ - u_z^- = \delta, \quad \sigma_{zz}^+ = \sigma_{zz}^-, \quad \sigma_{zr}^+ = \sigma_{zr}^-, \quad H_{zz}^+ = 0 \quad \text{for} \quad z = 0, \tag{12a}$$

$$\sigma_{zz}^+ = 0, \quad \sigma_{zr}^+ = 0, \quad H_{zz}^+ = 0 \quad \text{for} \quad z = h, \tag{12b}$$

where the superscripts "+" and "−", respectively, denote coating and substrate.

Because of non-torsional axisymmetry, all the quantities are only dependent on (r, z), and $\Psi_0 = \psi_0 = 0$. By using the zeroth-order Hankel transform technique, the potential functions can be set as

$$\Psi_j(r, z) = \int_0^\infty (A_{2j-1}\mathrm{e}^{\xi z_j} + A_{2j}\mathrm{e}^{-\xi z_j})J_0(\xi r)\mathrm{d}\xi, \quad j = 1, 2, 3, \tag{13a}$$

$$\psi_j(r, z) = \int_0^\infty A_{j+6}\mathrm{e}^{\xi z}J_0(\xi r)\mathrm{d}\xi, \quad j = 1, 2, \tag{13b}$$

where ξ is the Hankel transform parameter, and A_i are the coefficients to be determined by

boundary conditions. Inserting Eq. (13) into Eq. (3b) and then into Eq. (12), one gets

$$\sum_{j=1}^{6} A_j + \frac{A_7}{2\mu} = 0, \quad \sum_{j=1}^{3} \alpha_{1j}(A_{2j-1} - A_{2j})\xi - \frac{1}{2\mu}(A_j\xi - (3-4v)A_8) = \frac{\xi}{2\pi}, \tag{14a}$$

$$\sum_{j=1}^{3} \gamma_{1j}(A_{2j-1} + A_{2j})\xi = A_7\xi - 2(1-v)A_8, \tag{14b}$$

$$\sum_{j=1}^{3} s_j\gamma_{1j}(A_{2j-1} - A_{2j})\xi = A_7\xi - (1-2v)A_8, \tag{14c}$$

$$\sum_{j=1}^{3} \gamma_{2j}(A_{2j-1} + A_{2j}) = 0, \quad \sum_{j=1}^{3} \gamma_{1j}(A_{2j-1}\mathrm{e}^{\xi s_j h} + A_{2j}\mathrm{e}^{-\xi s_j h}) = 0, \tag{14d}$$

$$\sum_{j=1}^{3} s_j\gamma_{1j}(A_{2j-1}\mathrm{e}^{\xi s_j h} - A_{2j}\mathrm{e}^{-\xi s_j h}) = 0, \quad \sum_{j=1}^{3} \gamma_{2j}(A_{2j-1}\mathrm{e}^{\xi s_j h} + A_{2j}\mathrm{e}^{-\xi s_j h}) = 0. \tag{14e}$$

Thus, all the coefficients can be determined by solving Eq. (14), namely,

$$A_j = A_j^*(\ell), \quad j = 1, 2, \cdots, 7, \tag{15a}$$

$$A_8 = A_8^*(\ell)\xi, \tag{15b}$$

where $A_j^*(\ell)$ are functions of ℓ only, with $\ell = \exp(-h\xi)$.

Substituting these coefficients into Eqs. (3) and (7) yields the fundamental solutions of stresses in the coating and substrate. Here, it is worth noting that the obtained phason stress on the interface is zero, which implies that no phason stresses exist on the interface of a QC coating structure. That is, there are no phason SIFs at the interfacial crack tips. However, the coupling of phonon and phason fields is embedded in the material parameters ϑ_i, and these parameters can influence the SIFs and ERRs. Such a phenomenon is obviously different from that in ordinary crystal materials. As focus is on the interfacial fracture behavior, the field point is chosen to approach the crack face from the substrate. Therefore, we only give the expressions of stresses at an arbitrary field point (x, y, z) in the substrate.

When the Hankel transform parameter ξ approaches a sufficiently large value ξ_0, the parameter ℓ is close to zero. We have

$$\vartheta_1 = \lim_{\ell\to 0} A_7, \quad \vartheta_2\xi = \lim_{\ell\to 0} A_8, \tag{16}$$

where ϑ_i are material properties.

Inserting Eq. (16) into (13b), one obtains the potential functions in the substrate. As integrals cannot be analytically solved, the potential functions are rewritten as

$$\psi_1(r, z) = \int_0^{\infty} \vartheta_1\mathrm{e}^{\xi z}J_0(\xi r)\mathrm{d}\xi + \int_0^{\xi_0} (A_7 - \vartheta_1)\mathrm{e}^{\xi z}J_0(\xi r)\mathrm{d}\xi + E(1/\xi_0^2), \tag{17a}$$

$$\psi_2(r, z) = \int_0^{\infty} \vartheta_2\mathrm{e}^{\xi z}J_0(\xi r)\mathrm{d}\xi + \int_0^{\xi_0} (A_8 - \vartheta_2\xi)\mathrm{e}^{\xi z}J_0(\xi r)\mathrm{d}\xi + E(1/\xi_0^2), \tag{17b}$$

where $E(*)$ indicates the error of truncation. Integrals in Eq. (17) can be evaluated analytically or numerically. When ξ_0 is sufficiently large, the error is tiny. As shown in Fig. 3, when ξ_0 reaches $6/h$ and the values of coefficients keep unchanged, ξ_0 is selected as $10/h$ for a high accuracy in numerical calculation.

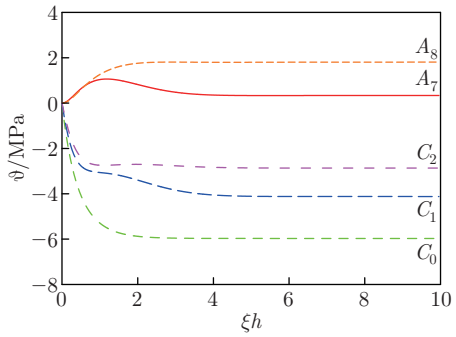

Fig. 3 Values of A_7, A_8, C_0, C_1, and C_2 versus ξ (color online)

Keep the formula $\int_0^\infty \mathrm{e}^{\xi z} J_0(\xi r)\mathrm{d}\omega = \frac{1}{\sqrt{r^2+z^2}}$ in mind. Then, Eq. (17) can be solved as

$$\psi_1(r,z) \approx \vartheta_1 \frac{1}{R} + \int_0^{\xi_0} (A_7 - \vartheta_1)\mathrm{e}^{\xi z} J_0(\xi r)\mathrm{d}\xi, \tag{18a}$$

$$\psi_2(r,z) \approx -\vartheta_2 \frac{z}{R^3} + \int_0^{\xi_0} (A_8 - \vartheta_2\xi)\mathrm{e}^{\xi z} J_0(\xi r)\mathrm{d}\xi, \tag{18b}$$

where $R = \sqrt{r^2+z^2} = \sqrt{(x-\zeta)^2+(y-\eta)^2+z^2}$.

Substituting Eq. (18) into Eq. (7a) yields stresses as

$$\Xi_1 = \sigma_{zz} = (2(1-v)\vartheta_2 - \vartheta_1)\frac{1}{R^3} + 3((1+2v)\vartheta_2 + \vartheta_1)\frac{z^2}{R^5} - 15\vartheta_2\frac{z^4}{R^7} + T_1 + zT_2, \tag{19a}$$

$$\Xi_2 = \sigma_{zx} = 3(\vartheta_1 + 2v\vartheta_2)\frac{xz}{R^5} - 15\vartheta_2\frac{xz^3}{R^7} + T_3 + zT_4, \tag{19b}$$

$$\Xi_3 = \sigma_{yz} = 3(\vartheta_1 + 2v\vartheta_2)\frac{xz}{R^5} - 15\vartheta_2\frac{yz^3}{R^7} + T_5 + zT_6, \tag{19c}$$

where the functions T_i are defined as

$$\begin{cases} T_1 = \displaystyle\int_0^{\xi_0} ((A_7 - \vartheta_1)\xi - 2(1-v)(A_8 - \vartheta_2\xi))\xi\mathrm{e}^{\xi z} J_0(\xi r)\mathrm{d}\xi, \\ T_2 = \displaystyle\int_0^{\xi_0} (A_8 - \vartheta_2\xi)\xi^2\mathrm{e}^{\xi z} J_0(\xi r)\mathrm{d}\xi, \\ T_3 = -\displaystyle\int_0^{\xi_0} ((A_7 - \vartheta_1)\xi - (1-2v)(A_8 - \vartheta_2\xi))\xi\mathrm{e}^{\xi z} J_1(\xi r)\mathrm{d}\xi \cdot \cos\phi, \\ T_4 = -\displaystyle\int_0^{\xi_0} (A_8 - \vartheta_2\xi)\xi^2\mathrm{e}^{\xi z} J_1(\xi r)\mathrm{d}\xi \cdot \cos\phi, \\ T_5 = -\displaystyle\int_0^{\xi_0} ((A_7 - \vartheta_1)\xi - (1-2v)(A_8 - \vartheta_2\xi))\xi\mathrm{e}^{\xi z} J_1(\xi r)\mathrm{d}\xi \cdot \sin\phi, \\ T_6 = -\displaystyle\int_0^{\xi_0} (A_8 - \vartheta_2\xi)\xi^2\mathrm{e}^{\xi z} J_1(\xi r)\mathrm{d}\xi \cdot \sin\phi. \end{cases} \tag{20}$$

According to Eq. (19), the anterior terms represent the effect of an infinite space with the same singularity, where the latter terms containing T_i reflect the effect of coating structure with a regular integrand. When the coating thickness is large enough, the functions T_i are

close to zero, and the solution is reduced to an infinite case. Similarly, one can get fundamental solutions for unit displacement discontinuities in the y- and x-directions, respectively, and for brevity, the detailed derivation is given in Appendices A and B.

4 Boundary integral-differential equations for interface cracks

Based on the fundamental solutions obtained above, one can construct the integral expressions for stresses at an arbitrary internal field point (x, y, z) in the substrate in terms of the displacement discontinuities across an interface crack S as

$$\sigma_{zx} = \int_S \{\Xi_8\|u_x\| + \Xi_5\|u_y\| + \Xi_2\|u_z\|\}\mathrm{d}S, \tag{21a}$$

$$\sigma_{yz} = \int_S \{\Xi_9\|u_x\| + \Xi_6\|u_y\| + \Xi_3\|u_z\|\}\mathrm{d}S, \tag{21b}$$

$$\sigma_{zz} = \int_S \{\Xi_7\|u_x\| + \Xi_4\|u_y\| + \Xi_1\|u_z\|\}\mathrm{d}S. \tag{21c}$$

As the filed point approaches the crack face, the integrals in Eq. (21) become hypersingular. Adopting finite-part integrals, the boundary integral-differential equations for an arbitrarily shaped crack S can be written as

$$\begin{aligned}\sigma_{zx}(x,y,0) = &\int_S \Big(\Big((\vartheta_4 - \vartheta_3 - (1-2v)\vartheta_5)\frac{1}{r^3} + 3\Big(\frac{1}{2}\vartheta_3 - \vartheta_4 + (1-2v)\vartheta_5\Big)\frac{\cos^2\phi}{r^3}\Big)\|u_x\| \\ &+ 3\Big(\frac{1}{2}\vartheta_3 - \vartheta_4 + (1-2v)\vartheta_5\Big)\frac{\sin\phi\cos\phi}{r^3}\|u_y\|\Big)\mathrm{d}S - 2\pi(\vartheta_1 + 2v\vartheta_2)\frac{\partial\|u_z\|}{\partial x} \\ &+ \int_S (T_{15}\|u_x\| + T_9\|u_y\| + T_3\|u_z\|)\mathrm{d}S,\end{aligned} \tag{22a}$$

$$\begin{aligned}\sigma_{yz}(x,y,0) = &\int_S \Big(3\Big(\frac{1}{2}\vartheta_3 - \vartheta_4 + (1-2v)\vartheta_5\Big)\frac{\sin\phi\cos\phi}{r^3}\|u_x\| \\ &+ \Big((\vartheta_4 - \vartheta_3 - (1-2v)\vartheta_5)\frac{1}{r^3} + 3\Big(\frac{1}{2}\vartheta_3 - \vartheta_4 + (1-2v)\vartheta_5\Big)\frac{\sin^2\phi}{r^3}\Big)\|u_y\|\Big)\mathrm{d}S \\ &- 2\pi(\vartheta_1 + 2v\vartheta_2)\frac{\partial\|u_z\|}{\partial y} + \int_S (T_9\|u_x\| + T_{11}\|u_y\| + T_5\|u_z\|)\mathrm{d}S,\end{aligned} \tag{22b}$$

$$\begin{aligned}\sigma_{zz}(x,y,0) = &(2(1-v)\vartheta_2 - \vartheta_1)\int_S \frac{1}{r^3}\|u_z\|\mathrm{d}S + 2\pi(\vartheta_4 - 2(1-v)\vartheta_5)\Big(\frac{\partial\|u_x\|}{\partial x} + \frac{\partial\|u_y\|}{\partial y}\Big) \\ &+ \int_S (T_{13}\|u_x\| + T_7\|u_y\| + T_1\|u_z\|)\mathrm{d}S,\end{aligned} \tag{22c}$$

where $r = \sqrt{(x-\zeta)^2 + (y-\eta)^2}$, $\cos\phi = (x-\zeta)/r$, and $\sin\phi = (y-\eta)/r$.

5 Green's functions for displacement discontinuities

The integral-differential equations in Eq. (22) are difficult to be analytically solved, especially for complex crack geometries and applied loads. Therefore, it is natural to resort to a displacement discontinuity boundary element method. Then, a rectangular element can be easily applied to discretize a crack of arbitrary shape, and its integral calculation is simple. Hence, a rectangular element is chosen, and the fundamental solutions are derived for the element subjected to uniform displacement discontinuities.

Let us assume that a rectangular element with length of $2a$ and width of $2b$ is centered at point (x_0, y_0). Over the element, uniform displacement discontinuities $\|u_x^e\|$, $\|u_y^e\|$, and $\|u_z^e\|$

are distributed. Thus, displacement discontinuities can be expressed by

$$\|u_i(x,y)\| = \|u_i^e\|S_r, \quad i = x, y, z, \tag{23}$$

where S_r is the domain function defined by the Heaviside function $H(x)$ as

$$S_r = (H(x+a) - H(x-a))(H(y+b) - H(y-b)). \tag{24}$$

Inserting Eq. (23) into Eq. (22), the stresses at the field point $(x, y, 0)$ caused by the e-th element can be obtained as

$$\sigma_{zx} = G_{11}\|u_x^e\| + G_{12}\|u_y^e\| + G_{13}\|u_z^e\|, \tag{25a}$$

$$\sigma_{yz} = G_{21}\|u_x^e\| + G_{22}\|u_y^e\| + G_{23}\|u_z^e\|, \tag{25b}$$

$$\sigma_{zz} = G_{31}\|u_x^e\| + G_{32}\|u_y^e\| + G_{33}\|u_z^e\|, \tag{25c}$$

where $G_{ij}(x, y)$ are Green's functions defined as

$$\begin{cases} G_{11} = (\vartheta_4 - \vartheta_3 - (1-2v)\vartheta_5)(I_1 + I_2) + 3\Big(\dfrac{1}{2}\vartheta_3 - \vartheta_4 + (1-2v)\vartheta_5\Big)I_1 + \displaystyle\int_{S_r} T_{15}\mathrm{d}S, \\ G_{12} = 3\Big(\dfrac{1}{2}\vartheta_3 - \vartheta_4 + (1-2v)\vartheta_5\Big)I_3 + \displaystyle\int_{S_r} T_9\mathrm{d}S, \\ G_{13} = \displaystyle\int_{S_r} T_3\mathrm{d}S - 2\pi(\vartheta_1 + 2v\vartheta_2)\frac{\partial S_r}{\partial x}, \\ G_{21} = 3\Big(\dfrac{1}{2}\vartheta_3 - \vartheta_4 + (1-2v)\vartheta_5\Big)I_3 + \displaystyle\int_{S_r} T_9\mathrm{d}S, \\ G_{22} = (\vartheta_4 - \vartheta_3 - (1-2v)\vartheta_5)(I_1 + I_2) + 3\Big(\dfrac{1}{2}\vartheta_3 - \vartheta_4 + (1-2v)\vartheta_5\Big)I_2 + \displaystyle\int_{S_r} T_{11}\mathrm{d}S, \\ G_{23} = \displaystyle\int_{S_r} T_5\mathrm{d}S - 2\pi(\vartheta_1 + 2v\vartheta_2)\frac{\partial S_r}{\partial y}, \\ G_{31} = \displaystyle\int_{S_r} T_{13}\mathrm{d}S + 2\pi(\vartheta_4 - 2(1-v)\vartheta_5)\frac{\partial S_r}{\partial x}, \\ G_{32} = \displaystyle\int_{S_r} T_7\mathrm{d}S + 2\pi(\vartheta_4 - 2(1-v)\vartheta_5)\frac{\partial S_r}{\partial y}, \\ G_{33} = (2(1-v)\vartheta_2 - \vartheta_1)(I_1 + I_2) + \displaystyle\int_{S_r} T_1\mathrm{d}S, \end{cases} \tag{26}$$

where kernel integrals I_i are defined in Eq. (15) in Ref. [39], where x_1 and x_2 respectively refer to x and y, and the partial differential formulas are defined as[39]

$$\begin{cases} \dfrac{\partial S_r}{\partial x} = (\delta(x+a) - \delta(x-a))(H(y+b) - H(y-b)), \\ \dfrac{\partial S_r}{\partial y} = (H(x+a) - H(x-a))(\delta(y+b) - \delta(y-b)), \end{cases} \tag{27}$$

in which δ is the delta function, and $\delta(x) = \mathrm{d}H(x)/\mathrm{d}x$.

6 SIFs and ERR

It is known that the terms containing the delta function cause the oscillatory singularity of stresses near the crack front[39]. According to Zhang and Wang[40], the delta function can be

approximated by the Gaussian distribution function, that is

$$\delta(x) = \frac{1}{\sqrt{2\pi}\varepsilon} \exp\Big(-\frac{x^2}{2\varepsilon^2}\Big), \tag{28}$$

where ε is the Gaussian parameter dependent on the geometry of a crack. In practical calculation[40], a relative value of $\varepsilon = 0.007\,5\ r_a$ is suitable, with the crack size r_a. After replacement, the point force induced by the delta function can be treated as a locally distributed load, and thus Eq. (22) can be converted into standard integral equations, where the terms converted from those containing the delta function no longer influence the singularity of stresses in the neighborhood of the crack front. In addition, the finite integral terms T_i reflecting coating effect do not influence the singularity of stresses near the crack front. Hence, the singularity index of stresses is $-1/2$, which is the same as that in a homogeneous medium.

An arbitrary point Q is chosen on the front of crack S. The Cartesian coordinate system $Oxyz$ is oriented so that the x- and y-directions are normal and tangent to the front, respectively. A local orthogonal, intrinsic coordinate system (n, τ, m) at point Q along the periphery of a planar crack is set up. The n-axis is perpendicular to the crack front line and is directed towards the inner side of a crack, while the τ-axis is tangential to the crack front line, and the m-axis is parallel to the global z-axis. Now let us introduce a local coordinate $(-\rho, 0, 0)$, where $\rho > 0$ outside the crack but close to point Q. By introducing the transformation

$$\zeta + \rho = r\cos\varphi, \quad \eta = r\sin\varphi, \tag{29}$$

the singular stresses at point $(-\rho, 0, 0)$ become

$$\begin{aligned}\sigma_{zx}(-\rho,0,0) = \int_S \Big(\Big((\vartheta_4-\vartheta_3-(1-2v)\vartheta_5)\frac{1}{r^3} + 3\Big(\frac{1}{2}\vartheta_3-\vartheta_4+(1-2v)\vartheta_5\Big)\frac{\cos^2\phi}{r^3}\Big)\|u_x\| \\ + 3\Big(\frac{1}{2}\vartheta_3-\vartheta_4+(1-2v)\vartheta_5\Big)\frac{\sin\phi\cos\phi}{r^3}\|u_y\|\Big)\mathrm{d}S, \end{aligned} \tag{30a}$$

$$\begin{aligned}\sigma_{yz}(-\rho,0,0) = \int_S \Big(3\Big(\frac{1}{2}\vartheta_3-\vartheta_4+(1-2v)\vartheta_5\Big)\frac{\sin\phi\cos\phi}{r^3}\|u_x\| \\ + \Big((\vartheta_4-\vartheta_3-(1-2v)\vartheta_5)\frac{1}{r^3} \\ + 3\Big(\frac{1}{2}\vartheta_3-\vartheta_4+(1-2v)\vartheta_5\Big)\frac{\sin^2\phi}{r^3}\Big)\|u_y\|\Big)\mathrm{d}S, \end{aligned} \tag{30b}$$

$$\sigma_{zz}(-\rho,0,0) = (2(1-v)\vartheta_2-\vartheta_1)\int_S \frac{1}{r^3}\|u_z\|\mathrm{d}S. \tag{30c}$$

Thus, the SIFs at the interface crack front are defined as

$$\begin{cases} K_{\mathrm{I}} = \lim\limits_{\rho\to 0}\sqrt{2\pi\rho}\sigma_{zz}(-\rho,0,0), \\ K_{\mathrm{II}} = \lim\limits_{\rho\to 0}\sqrt{2\pi\rho}\sigma_{zx}(-\rho,0,0), \\ K_{\mathrm{III}} = \lim\limits_{\rho\to 0}\sqrt{2\pi\rho}\sigma_{yz}(-\rho,0,0). \end{cases} \tag{31}$$

Inserting Eq. (30) into Eq. (31) yields

$$\begin{cases} K_{\mathrm{I}} = \sqrt{2\pi}\pi(2(1-v)\vartheta_2-\vartheta_1)\lim\limits_{\rho\to 0}\|u_z\|/\sqrt{\rho}, \\ K_{\mathrm{II}} = \sqrt{2\pi}\pi((1-2v)\vartheta_5-\vartheta_4)\lim\limits_{\rho\to 0}\|u_x\|/\sqrt{\rho}, \\ K_{\mathrm{III}} = -\sqrt{2\pi}\pi\vartheta_3\lim\limits_{\rho\to 0}\|u_y\|/\sqrt{\rho}, \end{cases} \tag{32}$$

where ρ denotes the distance to the crack front.

Based on the virtual crack closure method, one can derive the local ERR using the tractions and displacements ahead of the crack front[41]

$$G=\lim_{\Delta S\to 0}\frac{1}{2\Delta S}\int_{\Delta S}(\sigma_{zx}\|u_x\|+\sigma_{yz}\|u_y\|+\sigma_{zz}\|u_z\|)\mathrm{d}S, \tag{33}$$

and one obtains the final expressions of G in terms of SIFs as

$$G=\frac{1}{8\pi}\Big(\frac{K_{\mathrm{I}}^2}{2(1-v)\vartheta_2-\vartheta_1}+\frac{K_{\mathrm{II}}^2}{(1-2v)\vartheta_5-\vartheta_4}-\frac{K_{\mathrm{III}}^2}{\vartheta_3}\Big). \tag{34}$$

Here, the ERR G is related to three modes of SIFs, which can comprehensively reflect the fracture behavior.

7 Displacement discontinuity boundary element method

Let us consider an interface crack discretized into N rectangular elements. The displacement discontinuities are uniformly distributed within each element. Using the fundamental solutions from Eq. (25), we have

$$-p_x(x_i,y_i)=\sum_{e=1}^{N}(G_{11}\|u_x^e\|+G_{12}\|u_y^e\|+G_{13}\|u_z^e\|), \tag{35a}$$

$$-p_y(x_i,y_i)=\sum_{e=1}^{N}(G_{12}\|u_x^e\|+G_{22}\|u_y^e\|+G_{23}\|u_z^e\|), \tag{35b}$$

$$-p_z(x_i,y_i)=\sum_{e=1}^{N}(G_{31}\|u_x^e\|+G_{32}\|u_y^e\|+G_{33}\|u_z^e\|), \tag{35c}$$

where $i=1,2,3,\cdots,N$, and p_x, p_y, and p_z are the prescribed phonon tractions on crack faces. There are totally $3N$ equations and $3N$ corresponding discontinuities for a crack. After solving these linear algebraic equations, displacement discontinuities for each element can be obtained, and then stresses of a given point. Thus, the proposed displacement discontinuity boundary element method is flexible and suitable for complicated multi-crack problems with complex boundary conditions and geometries.

The displacement discontinuities close to the crack tip can be extrapolated by fitting the calculated results of elements near the crack front as

$$\|u_i\|=\beta_1^i\rho^{1/2}+\beta_2^i\rho^{3/2},\quad i=x,y,z, \tag{36}$$

where β_1^i and β_2^i are fitting coefficients, and ρ denotes the distance of a field point from the crack tip. Then, by substituting Eq. (36) into Eq. (32), the SIFs become

$$\begin{cases} K_{\mathrm{I}}=\sqrt{2\pi}\pi(2(1-v)\vartheta_2-\vartheta_1)\beta_1^z,\\ K_{\mathrm{II}}=\sqrt{2\pi}\pi(2(1-v)\vartheta_5-\vartheta_4)\beta_1^x,\\ K_{\mathrm{III}}=-\sqrt{2\pi}\pi\vartheta_3\beta_1^y. \end{cases} \tag{37}$$

Based on Eq. (34), the ERR can be calculated by fitting coefficients as

$$G=\frac{\pi^2}{4}((2(1-v)\vartheta_2-\vartheta_1)(\beta_1^z)^2+((1-2v)\vartheta_5-\vartheta_4)(\beta_1^x)^2-\vartheta_3(\beta_1^y)^2). \tag{38}$$

8 Results and discussion

In simulations, two kinds of 1D hexagonal QCs (QC1 and QC2) are selected, with relevant material constants[42]. The substrate material is aluminum (Al), and its shear modulus and Poisson's ratio are 30.5 GPa and 0.33, respectively. The displacement discontinuities, SIFs, and ERR are normalized by h, $p_z\sqrt{\pi h}$, and $p_z h$, respectively.

First, a rectangular interface crack with length L_1 and width L_2 under uniform tractions is studied. As shown in the calculation, the maximum values of SIFs and ERR all occur at the middle of the crack edge. Therefore, the middle points of four sides A, B, C, and D are selected to represent SIFs and ERR of the crack, and their positions are seen in Fig. 4. A rectangular crack is discretized by $n_1 \times n_2$ elements, where n_1 and n_2 are the numbers of discrete elements along the crack length and width, respectively.

8.1 Convergence analysis and validation of numerical simulation

First, the convergence is analyzed. The elements with 19×19, 39×39, and 49×49 are respectively used to discretize a rectangular interface crack. As shown in Fig. 5, high precision can already be reached with 39×39 elements. Meanwhile, to verify the proposed boundary element method (BEM), the results are compared with simulations by COMSOL software. Based on the comparison of crack opening displacement distribution, it is shown that the relevant results are consistent with each other, which to some extent confirms the proposed method.

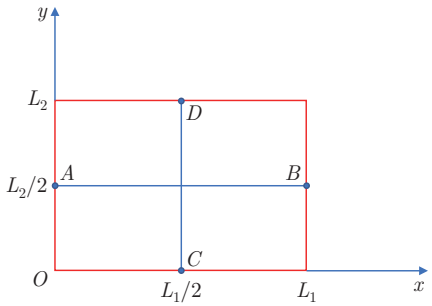

Fig. 4 Schematic representation of rectangular crack at interface (color online)

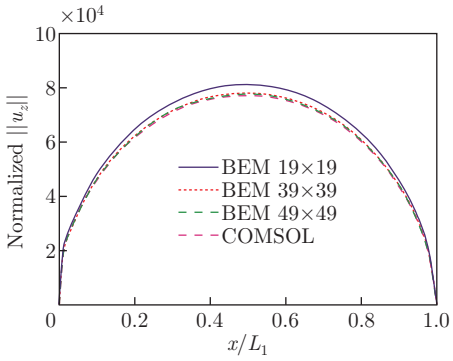

Fig. 5 Normalized displacement discontinuity $\|u_z\|$ along $y = L_2/2$ of crack with fixed ratios of $L_1/h = 2$ and $L_1/L_2 = 1$ for different element numbers (color online)

8.2 Normalized displacement discontinuity distribution under different loads

As observed in Fig. 6, the displacement discontinuity $\|u_x\|$ is symmetric along $y = L_2/2$ and anti-symmetric along $x = L_1/2$, while the symmetry of $\|u_y\|$ is in contrast, and $\|u_z\|$ is symmetric along both. It is obvious that the induced $\|u_z\|$ is one order of magnitude higher than $\|u_z\|$ and $\|u_y\|$. For mixed loads, the distribution of discontinuities will be more complex.

8.3 Influence of ratio, material mismatch, and crack length-width ratio

As shown in Fig. 7, the absolute values of SIFs and ERR increase with increasing L_1/h. The variation tendencies of SIFs are different, especially for K_{II} with negative values, meaning that the direction is opposite to the definition direction. As a comprehensive fracture parameter, G is an embodiment of K_{I}, K_{II}, and K_{III}, which can better reflect the fracture behavior of cracks than a single SIF. In addition, the material mismatch also has an important influence on the fracture behavior. Although there are no phason tractions applied, the influence by a phason

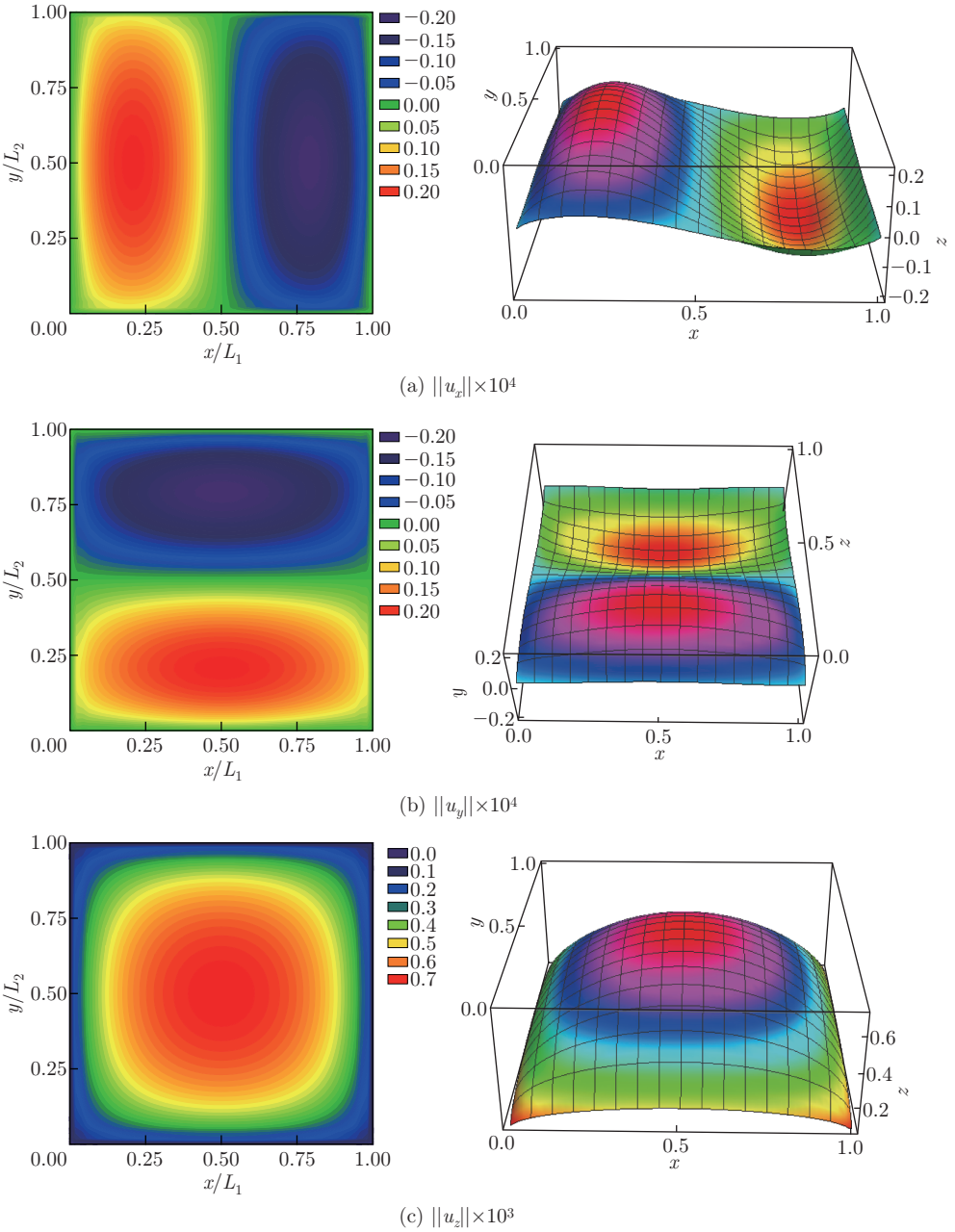

Fig. 6 Normalized displacement discontinuities on a crack with $L_1/h = 2$ and $L_1/L_2 = 1$ for QC1 coating under $p_z = 10\,\text{MPa}$ (color online)

field cannot be ignored, because different QC materials possess obvious discrepant SIFs and ERRs.

The effect of length-width ratio of rectangular crack L_2/L_1 on the fracture is also studied. As shown in Fig. 8, when L_2/L_1 is less than 1, the values of K_I at points A, B, C, and D all increase with the increasing of L_2/L_1. When $L_2/L_1 = 1$, K_I at points A and C is equal, while that at points B and D is equal. As L_2/L_1 continues to increase, K_I at points C and D

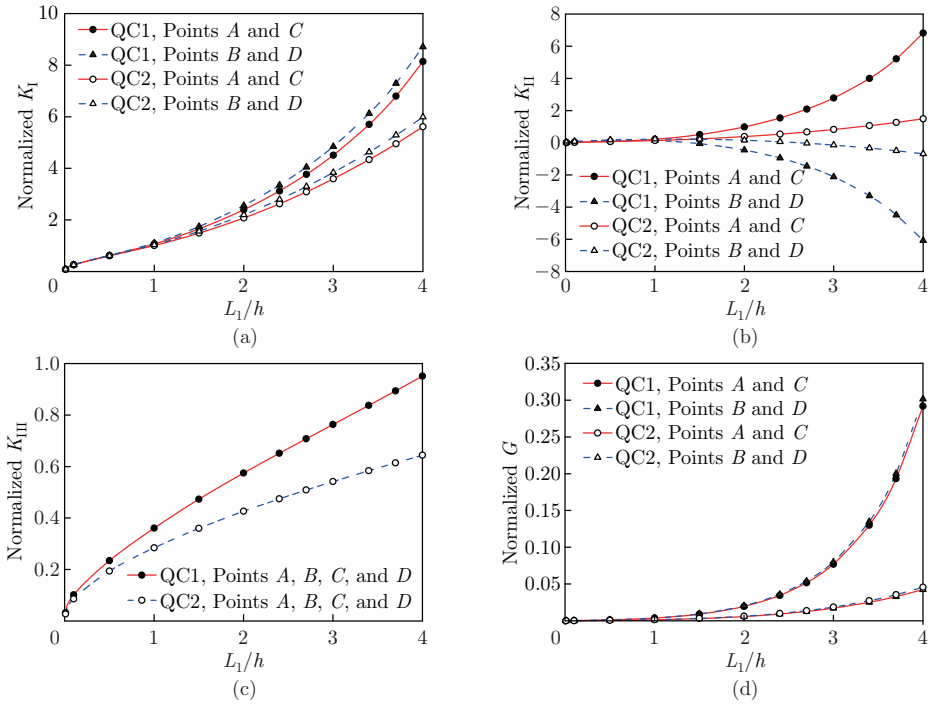

Fig. 7 Normalized SIFs and ERR at midpoints of crack sides versus the ratio L_1/h for different material mismatches with $L_1 = L_2$ under $p_x = 10\,\mathrm{MPa}$, $p_y = 10\,\mathrm{MPa}$, and $p_z = 50\,\mathrm{MPa}$ (color online)

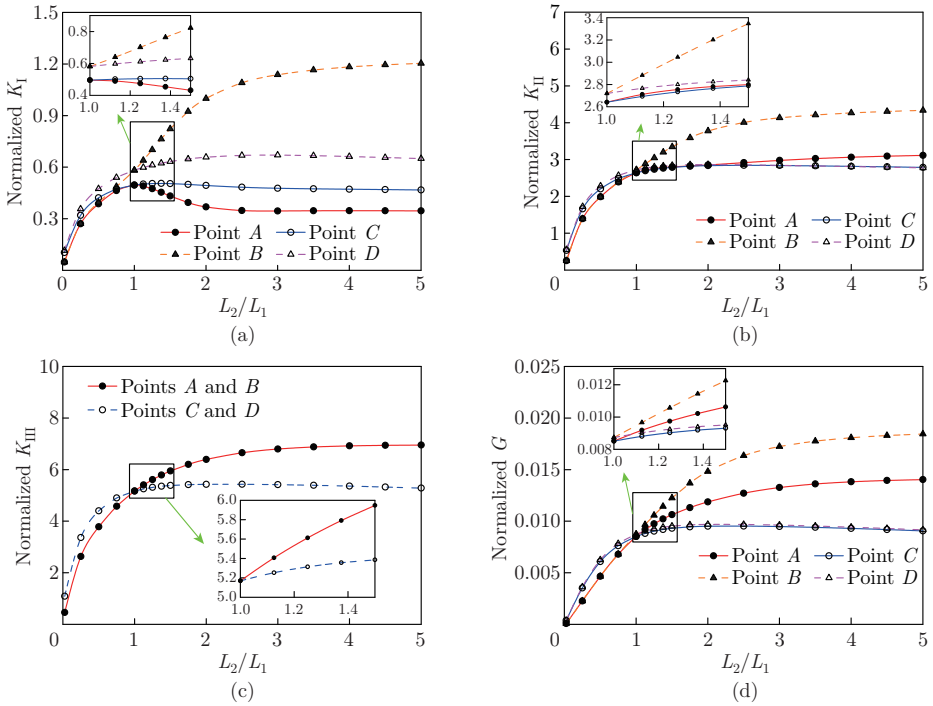

Fig. 8 Normalized SIFs and ERR at midpoints of crack sides versus the ratio L_2/L_1 under $p_x = 50\,\mathrm{MPa}$, $p_y = 50\,\mathrm{MPa}$, and $p_z = 10\,\mathrm{MPa}$ (color online)

increases slightly and is basically stable after 2.5, while K_{I} decreases at point A and increases at point B, and they gradually tend to be stable. In addition, K_{II}, K_{III}, and G at points A, B, C, and D all increase and tend to be stable with the increase of L_2/L_1. When $L_2/L_1 < 1$, their values at points C and D are larger than those at points A and B, while when $L_2/L_1 > 1$, their values at points A and B are larger than those at points C and D. When $L_2/L_1 > 1$, point B is the most dangerous among four points, followed by point A, and points C and D are close and safest. Here, the effect of length-width ratio shows that, a planar crack in a 3D problem cannot be simply reduced as a line crack in a 2D case. In general cases, a 3D mathematical model can better reflect the actual working condition, and a reduced 2D problem cannot mirror an overall fracture performance precisely.

8.4 Influence of applied loads

As shown in Fig. 9, K_{I} and K_{II} at points A and B and K_{III} at points C and D are not related to p_y. Only K_{I} and K_{II} at points C and D and K_{III} at points A and B change linearly with p_y, and they are not only related to the applied value of p_y, but also to its direction. Meanwhile, the ERR increases nonlinearly with the increase of p_y, and the relative value of loads may change the most dangerous points. When p_y is large enough compared to p_x and p_z, points A and B are more dangerous than points C and D.

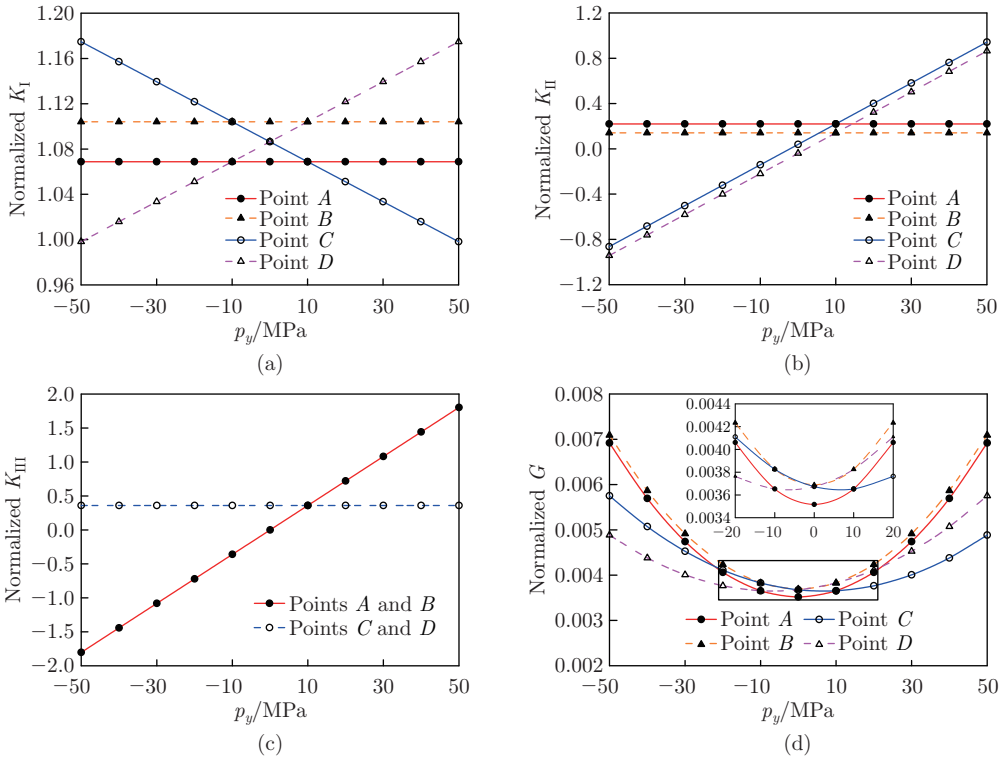

Fig. 9 Normalized SIFs and ERR at midpoints of crack sides versus p_y under $p_x = 10\,\mathrm{MPa}$ and $p_z = 50\,\mathrm{MPa}$ (color online)

9 Conclusions

In this paper, the displacement discontinuity method has been extended to study the 3D interfacial cracks in a 1D hexagonal QC coating structure. The fundamental solutions of concentrated displacement discontinuities are derived, and the boundary integral-differential equations

are constructed for an arbitrarily shaped crack. A corresponding boundary element method is proposed, and Green's functions of rectangular element with uniform displacement discontinuities are derived. Several main conclusions are drawn.

(i) Different from a 2D problem, the 3D interface crack problem of QC coating is more complex, which can reflect the actual working situation.

(ii) When the ratio of crack size to coating thickness grows, SIFs and ERR increase, and the rectangular crack expands to be circular.

(iii) The material mismatch, applied loads, and crack shape exhibit a significant influence on the interfacial fracture of QC coating.

The present work lays a foundation for the further 3D fracture analysis of QC and other intelligent materials with coating structures.

References

[1] SHECHTMAN, D., BLECH, I., GRATIAS, D., and CAHN, J. W. Metallic phase with long-range orientational order and no translational symmetry. *Physical Review Letters*, **53**, 1951–1953 (1984)

[2] DUBOIS, J. M. Properties and applications of quasicrystals and complex metallic alloys. *Chemical Society Reviews*, **41**, 6760–6777 (2012)

[3] WOLF, W., SCHULZ, R., SAVOIE, S., BOLFARINI, C., KIMINAMI, C. S., and BOTTA, E. J. Structural, mechanical and thermal characterization of an Al-Co-Fe-Cr alloy for wear and thermal barrier coating applications. *Surface & Coatings Technology*, **319**, 241–248 (2017)

[4] DUBOIS, J. M., KANG, S. S., and STEBUT, J. V. Quasicrystalline low-friction coatings. *Journal of Materials Science Letters*, **10**, 537–541 (1991)

[5] DUBOIS, J. M. New prospects from potential applications of quasicrystalline materials. *Materials Science and Engineering A*: *Structural Materials Properties Microstructure and Processing*, **294**, 4–9 (2000)

[6] UCHIDA, N. A review of thermal barrier coatings for improvement in thermal efficiency of both gasoline and diesel reciprocating engines. *International Journal of Engine Research*, **23**, 3–19 (2022)

[7] ZHOU, C. G., CAI, R., GONG, S. K., and XU, H. B. Hot corrosion of AlCuFeCr quasicrystalline coating on titanium alloys with NaCl deposit. *Surface & Coatings Technology*, **201**, 1718–1723 (2006)

[8] MOHSENI, M., RECLA, L., MORA, J., GALLEGO, P. G., AGUERO, A., and GOLOVIN, K. Quasicrystalline coatings exhibit durable low interfacial toughness with ice. *ACS Applied Materials & Interfaces*, **13**, 36517–36526 (2021)

[9] MORA, J., GARCIA, P., MUELAS, R., and AGUERO, A. Hard quasicrystalline coatings deposited by HVOF thermal spray to reduce ice accretion in aero-structures components. *Coatings*, **10**, 290 (2020)

[10] WOLF, W., BOLFARINI, C., KIMINAMI, C. S., and BOTTA, W. J. Recent developments on fabrication of Al-matrix composites reinforced with quasicrystals: from metastable to conventional processing. *Journal of Materials Research*, **36**, 281–297 (2021)

[11] NAYAK, C., AGHAJAMALI, A., SOLAIMANI, M., RAKSHIT, J. K., PANIGRAHY, D., KUMAR, K. V. P., and RAMAKRISHNA, B. Dodecanacci superconductor-metamaterial photonic quasicrystal. *Optik*, **222**, 165290 (2020)

[12] HUTTUNEN-SAARIVIRTA, E. Microstructure, fabrication and properties of quasicrystalline Al-Cu-Fe alloys: a review. *Journal of Alloys and Compounds*, **363**, 150–174 (2004)

[13] PARSAMEHR, H., CHEN, T. S., WANG, D. S., LEU, M. S., HAN, I., XI, Z. C., TSAI, A. P., SHAHANI, A. J., and LAI, C. H. Thermal spray coating of Al-Cu-Fe quasicrystals: dynamic observations and surface properties. *Materialia*, **8**, 100432 (2019)

[14] SOUZA, T. A., SILVA, D. D. S., JUNIOR, F. W. E. L. A., FEITOSA, F. R. P., GOMES, R. M., and LIMA, B. A. S. G. Analysis of the surface properties of Al-Cu-Fe-B and Al-Co-Cu quasicrystalline coatings produced by HVOF. *MRS Communications*, **11**, 873–878 (2021)

[15] LIU, X. Q., WU, Y. S., QIU, Z. G., LU, Z. Y., YAO, S. Q., ZHUO, S. Y., and ZENG, D. C. Simultaneously enhancing wear and corrosion resistance of HVAF-sprayed Fe-based amorphous coating from Mo clad feedstock. *Journal of Materials Processing Technology*, **302**, 117465 (2022)

[16] CAI, M. W. and SHEN, J. Phase transformation of high velocity air fuel (HVAF)-sprayed Al-Cu-Fe-Si quasicrystalline coating. *Metals*, **10**, 834 (2020)

[17] FU, Y. Q., KANG, N., LIAO, H. L., GAO, Y., and CODDET, C. An investigation on selective laster melting of Al-Cu-Fe-Cr quasicrystal: from single layer to multilayers. *Intermetallics*, **86**, 51–58 (2017)

[18] POLISHCHUK, S., USTINOV, A., TELYCHKO, V., MERSTALLINGER, A., MOZDZEN, G., and MELNICHENKO, T. Fabrication of thick, crack-free quasicrystalline Al-Cu-Fe coatings by electron-beam deposition. *Surface & Coatings Technology*, **291**, 406–412 (2016)

[19] FEITOSA, F. R. P., GOMES, R. M., SILVA, M. M. R., DE LIMA, S. J. G., and DUBOIS, J. M. Effect of oxygen/fuel ratio on the microstructure and properties of HVOF-sprayed $Al_{59}Cu_{25.5}Fe_{12.5}B_3$ quasicrystalline coatings. *Surface & Coatings Technology*, **353**, 171–178 (2018)

[20] XIAO, M., LIU, X. Q., ZENG, S. H., ZHENG, Z. G., WANG, G., QIU, Z. G., LIU, M., and ZENG, D. C. Effects of particle size on the microstructure and mechanical properties of HVAF-sprayed Al-based quasicrystalline coatings. *Journal of Thermal Spray Technology*, **30**, 1380–1392 (2021)

[21] CHENG, J., WU, Y. P., HONG, S., CHENG, J. B., QIAO, L., WANG, Y. J., and ZHU, S. S. Spray parameters optimization, microstructure and corrosion behavior of high-velocity oxygen-fuel sprayed non-equiatomic CuAlNiTiSi medium-entropy alloy coatings. *Intermetallics*, **142**, 107442 (2022)

[22] BANDYOPADHYAY, P. P., HADAD, M., JAEGGI, C., and SIEGMANN, S. Microstructural, tribological and corrosion aspects of thermally sprayed Ti-Cr-Si coatings. *Surface & Coatings Technology*, **203**, 35–45 (2008)

[23] SANCHEZ, A., DE BLAS, F. J., ALGABA, J. M., ALVAREZ, J., VALLES, P., GARCIA-POGGIO, M. C., and AGUERO, A. Application of quasicrystalline materials as thermal barriers in aeronautics and future perspectives of use for these materials. *Materials Research Society Symposium Proceedings*, **553**, 447–458 (1999)

[24] FAN, T. Y., TANG, Z. Y., and CHEN, W. Q. Theory of linear, nonlinear and dynamic fracture for quasicrystals. *Engineering Fracture Mechanics*, **82**, 185–194 (2012)

[25] SUN, T. Y., GUO, J. H., and PAN, E. Nonlocal vibration and buckling of two-dimensional layered quasicrystal nanoplates embedded in an elastic medium. *Applied Mathematics and Mechanics* (*English Edition*), **42**(8), 1077–1094 (2021) https://doi.org/10.1007/s10483-021-2743-6

[26] LI, L. H., CUI, X. W., and GUO, J. H. Interaction between a screw dislocation and an elliptical hole with two asymmetrical cracks in a one-dimensional hexagonal quasicrystal with piezoelectric effect. *Applied Mathematics and Mechanics* (*English Edition*), **41**(6), 899–908 (2020) https://doi.org/10.1007/s10483-020-2615-6

[27] ZHANG, M., GUO, J. H., and LI, Y. S. Bending and vibration of two-dimensional decagonal quasicrystal nanoplates via moddified couple-stress theory. *Applied Mathematics and Mechanics* (*English Edition*), **43**(3), 371–388 (2022) https://doi.org/10.1007/s10483-022-2818-6

[28] YANG, L. Z., LI, Y., GAO, Y., PAN, E. N., and WAKSMANSKI, N. Three-dimensional exact electric-elastic analysis of a multilayered two-dimensional decagonal quasicrystal plate subjected to patch loading. *Composite Structures*, **171**, 198–216 (2017)

[29] HUANG, Y. Z., LI, Y., ZHANG, L. L., ZHANG, H., and GAO, Y. Dynamic analysis of a multilayered piezoelectric two-dimensional quasicrystal cylindrical shell filled with compressible fluid using the state-space approach. *Acta Mechanica*, **231**, 2351–2368 (2020)

[30] HOU, P. F., CHE, B. J., and ZHANG, Y. An accurate and efficient analytical method for 1D hexagonal quasicrystal coating under the tangential force based on the Green's function. *International Journal of Mechanical Sciences*, **131**, 982–1000 (2017)

[31] HUANG, R. K., DING, S. H., CHEN, Q. W. L., LYU, C. F., ZHANG, X., and LI, X. Sliding frictional contact of one dimensional hexagonal piezoelectric quasicrystals coating on piezoelectric substrate with imperfect interface. *International Journal of Solids and Structures*, **239**, 111423 (2022)

[32] FAN, T. Y., XIE, L. Y., FAN, L., and WANG, Q. Z. Interface of quasicrystal and crystal. *Chinese Physics B*, **20**, 076102 (2011)

[33] DANG, H. Y., LYU, S. Y., FAN, C. Y., LU, C. S., REN, J. L., and ZHAO, M. H. Analysis of anti-plane interface cracks in one-dimensional hexagonal quasicrystal coating. *Applied Mathematical Modelling*, **81**, 641–652 (2020)

[34] ZHAO, M. H., FAN, C. Y., LU, C. S., and DANG, H. Y. Interfacial fracture analysis for a two-dimensional decagonal quasi-crystal coating layer structure. *Applied Mathematics and Mechanics* (*English Edition*), **42**, 1633–1648 (2021) https://doi.org/10.1007/s10483-021-2786-5

[35] CROUCH, S. L. Solution of plane elasticity problems by the displacement discontinuity method. I. Infinite body solution. *International Journal for Numerical Methods in Engineering*, **10**, 301–343 (1976)

[36] CHEN, W. Q., MA, Y. L., and DING, H. J. On three-dimensional elastic problems of one-dimensional hexagonal quasicrystal bodies. *Mechanics Research Communications*, **31**, 633–641 (2004)

[37] HOU, P. F., JIANG, H. Y., and LI, Q. H. Three-dimensional steady-state general solution for isotropic thermoelastic materials with applications I: general solutions. *Journal of Thermal Stresses*, **36**, 727–747 (2013)

[38] ZHAO, M. H., CHENG, C. J., and LIU, Y. J. Moment stress intensity factors for collinear and parallel cracks in Reissner's plate: boundary integral equation approach. *Theoretical and Applied Fracture Mechanics*, **22**, 261–266 (1995)

[39] ZHAO, Y. F., ZHAO, M. H., PAN, E. N., and FAN, C. Y. Green's functions and extended displacement discontinuity method for interfacial cracks in three-dimensional transversely isotropic magneto-electro-elastic bi-materials. *International Journal of Solids and Structures*, **52**, 56–71 (2015)

[40] ZHANG, A. B. and WANG, B. L. An opportunistic analysis of the interface crack based on the modified interface dislocation method. *International Journal of Solids and Structures*, **50**, 15–20 (2013)

[41] TANG, R. J., CHEN, M. C., and YUE, J. C. Theoretical analysis of three-dimensional interface crack. *Science in China Series A*: *Mathematics*, **41**, 443–448 (1998)

[42] DANG, H. Y., ZHAO, M. H., FAN, C. Y., and CHEN, Z. T. Analysis of a three-dimensional arbitrarily shaped interface crack in a one-dimensional hexagonal thermo-electro-elastic quasicrystal bi-material, part 2: numerical method. *Engineering Fracture Mechanics*, **180**, 268–281 (2017)

Appendix A Fundamental solution for concentrated $\|\boldsymbol{u_y}\| = \boldsymbol{\delta}$

When $\|u_y\| = \delta$ is applied at the interfacial point $(\zeta, \eta, 0)$, the boundary conditions are

$$\begin{cases} u_r^+ - u_r^- = \delta \sin\phi, \quad u_\phi^+ - u_\phi^- = \delta\cos\phi, \\ u_z^+ = u_z^-, \quad \sigma_{zz}^+ = \sigma_{zz}^-, \quad \sigma_{zr}^+ = \sigma_{zr}^-, \quad \sigma_{z\phi}^+ = \sigma_{z\phi}^-, \quad H_{zz}^+ = 0 \quad \text{for} \quad z = 0, \end{cases} \tag{A1a}$$

$$\sigma_{zz}^+ = 0, \quad \sigma_{zr}^+ = 0, \quad \sigma_{z\phi}^+ = 0, \quad H_{zz}^+ = 0 \quad \text{for} \quad z = h. \tag{A1b}$$

Based on the first-order Hankel transform technique, the potential functions are assumed as

$$\Psi_0 = \int_0^\infty (B_1 \mathrm{e}^{\xi z_0} + B_2 \mathrm{e}^{-\xi z_0}) J_1(\xi r) \mathrm{d}\xi \cdot \cos\phi, \tag{A2a}$$

$$\Psi_j = \int_0^\infty (B_{2j+1} \mathrm{e}^{\xi z_j} + B_{2j+2} \mathrm{e}^{-\xi z_j}) J_1(\xi r) \mathrm{d}\xi \cdot \sin\phi \quad \text{for} \quad j = 1, 2, 3 \tag{A2b}$$

$$\psi_0 = \int_0^\infty C_0 \mathrm{e}^{\xi z} J_1(\xi r) \mathrm{d}\xi \cdot \cos\phi, \tag{A2c}$$

$$\psi_j = \int_0^\infty C_j \mathrm{e}^{\xi z} J_1(\xi r) \mathrm{d}\xi \cdot \sin\phi \quad \text{for} \quad j = 1, 2, \tag{A2d}$$

where $\cos\phi = (x-\zeta)/r$, and $\sin\phi = (y-\eta)/r$. Inserting Eq. (A2) into Eqs. (3b) and (7b), and then substituting them into Eq. (A1), all the coefficients can be obtained, namely,

$$B_j = B_j^*(\ell), \quad j = 1 \sim 8, \tag{A3a}$$

$$C_0 = C_0^*(\ell), \quad C_1 = C_1^*(\ell), \quad C_2 = C_2^*(\ell)\xi. \tag{A3b}$$

Similarly, when the Hankel transform parameter ξ approaches a sufficiently large value ξ_0, we have the following limit values:

$$\vartheta_3 = \lim_{\ell \to 0} C_0, \quad \vartheta_4 = \lim_{\ell \to 0} C_1, \quad \vartheta_5 \xi = \lim_{\ell \to 0} C_2. \tag{A4}$$

Then, one obtains the potential functions in substrate as

$$\begin{cases} \psi_0 = \vartheta_3 \dfrac{1}{r}\Big(1 + \dfrac{z}{R}\Big) \cdot \cos\phi + \displaystyle\int_0^{\xi_0} (C_0 - \vartheta_3) \mathrm{e}^{\xi z} J_1(\xi r) \mathrm{d}\xi \cdot \cos\phi, \\ \psi_1 = \vartheta_4 \dfrac{1}{r}\Big(1 + \dfrac{z}{R}\Big) \cdot \sin\phi + \displaystyle\int_0^{\xi_0} (C_1 - \vartheta_4) \mathrm{e}^{\xi z} J_1(\xi r) \mathrm{d}\xi \cdot \sin\phi, \\ \psi_2 = \vartheta_5 \dfrac{r}{R^3} \cdot \sin\phi + \displaystyle\int_0^{\xi_0} (C_2 - \vartheta_5 \xi) \mathrm{e}^{\xi z} J_1(\xi r) \mathrm{d}\xi \cdot \sin\phi. \end{cases} \tag{A5}$$

Inserting Eq. (A5) into general solutions, the induced stresses in substrate are

$$\begin{cases} \Xi_4 = \sigma_{zz} = -3(\vartheta_4 - 2(1-v)\vartheta_5) \dfrac{yz}{R^5} + 15\vartheta_5 \dfrac{yz^3}{R^7} + T_7 + zT_8, \\ \Xi_5 = \sigma_{zx} = 3\Big(\dfrac{1}{2}\vartheta_3 - \vartheta_4 + (1-2v)\vartheta_5\Big) \dfrac{xy}{R^5} + 15\vartheta_5 \dfrac{xyz^2}{R^7} + T_9 + zT_{10}, \\ \Xi_6 = \sigma_{yz} = (\vartheta_4 - \vartheta_3 - (1-2v)\vartheta_5) \dfrac{1}{R^3} + 3\Big(\dfrac{1}{2}\vartheta_3 - \vartheta_4 + (1-2v)\vartheta_5\Big) \dfrac{y^2}{R^5} \\ \qquad + 3\Big(\dfrac{1}{2}\vartheta_3 - \vartheta_5\Big) \dfrac{z^2}{R^5} + 15\vartheta_5 \dfrac{y^2 z^2}{R^7} + T_{11} + zT_{12}, \end{cases} \tag{A6}$$

where

$$\begin{cases} T_7 = \displaystyle\int_0^{\xi_0} ((C_1 - \vartheta_4)\xi - 2(1-v)(C_2 - \vartheta_5\xi)) \xi \mathrm{e}^{\xi z} J_1(\xi r) \mathrm{d}\xi \cdot \sin\phi, \\ T_8 = \displaystyle\int_0^{\xi_0} (C_2 - \vartheta_5\xi) \xi^2 \mathrm{e}^{\xi z} J_1(\xi r) \mathrm{d}\xi \cdot \sin\phi, \\ T_9 = \displaystyle\int_0^{\xi_0} \Big(\frac{1}{2}(C_0 - \vartheta_3)\xi - (C_1 - \vartheta_4)\xi + (1-2v)(C_2 - \vartheta_5\xi)\Big) \xi \mathrm{e}^{\xi z} J_2(\xi r) \mathrm{d}\xi \cdot \sin\phi\cos\phi, \\ T_{10} = -\displaystyle\int_0^{\xi_0} (C_2 - \vartheta_5\xi) \xi^2 \mathrm{e}^{\xi z} J_2(\xi r) \mathrm{d}\xi \cdot \sin\phi\cos\phi, \\ T_{11} = \dfrac{1}{2}\displaystyle\int_0^{\xi_0} \Big(\frac{1}{2}(C_0 - \vartheta_3)\xi + (C_1 - \vartheta_4)\xi - (1-2v)(C_2 - \vartheta_5\xi)\Big) \xi \mathrm{e}^{\xi z} J_0(\xi r) \mathrm{d}\xi \\ \qquad - \dfrac{1}{2}\displaystyle\int_0^{\xi_0} \Big(\frac{1}{2}(C_0 - \vartheta_3)\xi - (C_1 - \vartheta_4)\xi + (1-2v)(C_2 - \vartheta_5\xi)\Big) \xi \mathrm{e}^{\xi z} J_2(\xi r) \mathrm{d}\xi \cdot \cos(2\phi), \\ T_{12} = \dfrac{1}{2}\displaystyle\int_0^{\xi_0} (C_2 - \vartheta_5\xi) \xi^2 \mathrm{e}^{\xi z} J_0(\xi r) \mathrm{d}\xi + \dfrac{1}{2}\int_0^{\xi_0} (C_2 - \vartheta_5\xi) \xi^2 \mathrm{e}^{\xi z} J_2(\xi r) \mathrm{d}\xi \cdot \cos(2\phi). \end{cases} \tag{A7}$$

Appendix B Fundamental solution for concentrated $\|\boldsymbol{u_x}\| = \boldsymbol{\delta}$

When $\|u_x\| = \delta$ is applied, the corresponding boundary conditions are

$$\begin{cases} u_r^+ - u_r^- = \delta(r)\cos\phi, \quad u_\phi^+ - u_\phi^- = \delta(r)\sin\phi, \\ u_z^+ - u_z^- = 0, \quad \sigma_{zz}^+ - \sigma_{zz}^- = 0, \quad \sigma_{zr}^+ - \sigma_{zr}^- = 0, \\ \sigma_{z\phi}^+ - \sigma_{z\phi}^- = 0, \quad H_{zz}^+ = 0 \quad \text{for} \quad z = 0, \end{cases} \tag{B1a}$$

$$\sigma_{zz}^+ = 0, \quad \sigma_{zr}^+ = 0, \quad \sigma_{z\phi}^+ = 0, \quad H_{zz}^+ = 0 \quad \text{for} \quad z = h. \tag{B1b}$$

By simply converting trigonometric functions, potential functions can be assumed as

$$\begin{cases} \psi_0 = -\vartheta_3 \dfrac{1}{r}\Big(1 + \dfrac{z}{R}\Big) \cdot \sin\phi - \displaystyle\int_0^{\xi_0} (C_0 - \vartheta_3)\mathrm{e}^{\xi z} J_1(\xi r)\mathrm{d}\xi \cdot \sin\phi, \\ \psi_1 = \vartheta_4 \dfrac{1}{r}\Big(1 + \dfrac{z}{R}\Big) \cdot \sin\phi + \displaystyle\int_0^{\xi_0} (C_1 - \vartheta_4)\mathrm{e}^{\xi z} J_1(\xi r)\mathrm{d}\xi \cdot \cos\phi, \\ \psi_2 = \vartheta_5 \dfrac{r}{R^3} \cdot \cos\phi + \displaystyle\int_0^{\xi_0} (C_2 - \vartheta_5\xi)\mathrm{e}^{\xi z} J_1(\xi r)\mathrm{d}\xi \cdot \cos\phi. \end{cases} \tag{B2}$$

Then, the stresses of an arbitrary point (x, y, z) in substrate are obtained as

$$\begin{cases} \Xi_7 = \sigma_{zz} = -3(\vartheta_4 - (1-2v)\vartheta_5)\dfrac{xz}{R^5} + 15\vartheta_5 \dfrac{xz^3}{R^7} + T_{13} + zT_{14}, \\ \Xi_8 = \sigma_{zx} = (\vartheta_4 - \vartheta_3 - (1-2v)\vartheta_5)\dfrac{1}{R^3} + 3\Big(\dfrac{1}{2}\vartheta_3 - \vartheta_4 + (1-2v)\vartheta_5\Big)\dfrac{x^2}{R^5} \\ \qquad\quad + 3\Big(\dfrac{1}{2}\vartheta_3 - \vartheta_5\Big)\dfrac{z^2}{R^5} + 15\vartheta_5 \dfrac{x^2 z^2}{R^7} + T_{15} + zT_{16}, \\ \Xi_9 = \sigma_{yz} = 3\Big(\dfrac{1}{2}\vartheta_3 - \vartheta_4 + (1-2v)\vartheta_5\Big)\dfrac{xy}{R^5} + 15\vartheta_5 \dfrac{xyz^2}{R^7} + T_9 + zT_{10}, \end{cases} \tag{B3}$$

where the arisen functions are defined as

$$\begin{cases} T_{13} = \displaystyle\int_0^{\xi_0} ((C_1 - \vartheta_4)\xi - 2(1-v)(C_2 - \vartheta_5\xi))\xi \mathrm{e}^{\xi z} J_1(\xi r)\mathrm{d}\xi \cdot \cos\phi, \\ T_{14}(r, \phi, z) = \displaystyle\int_0^{\xi_0} (C_2 - \vartheta_5\xi)\xi^2 \mathrm{e}^{\xi z} J_1(\xi r)\mathrm{d}\xi \cdot \cos\phi, \\ T_{15} = \dfrac{1}{2}\displaystyle\int_0^{\xi_0} \Big(\dfrac{1}{2}(C_0 - \vartheta_3)\xi + (C_1 - \vartheta_4)\xi - (1-2v)(C_2 - \vartheta_5\xi)\Big)\xi \mathrm{e}^{\xi z} J_0(\xi r)\mathrm{d}\xi \\ \qquad\quad + \dfrac{1}{2}\displaystyle\int_0^{\xi_0} \Big(\dfrac{1}{2}(C_0 - \vartheta_3)\xi - (C_1 - \vartheta_4)\xi + (1-2v)(C_2 - \vartheta_5\xi)\Big)\xi \mathrm{e}^{\xi z} J_2(\xi r)\mathrm{d}\xi \cdot \cos(2\phi), \\ T_{16} = \dfrac{1}{2}\displaystyle\int_0^{\xi_0} (C_2 - \vartheta_5\xi)\xi^2 \mathrm{e}^{\xi z} J_0(\xi r)\mathrm{d}\xi - \dfrac{1}{2}\displaystyle\int_0^{\xi_0} (C_2 - \vartheta_5\xi)\xi^2 \mathrm{e}^{\xi z} J_2(\xi r)\mathrm{d}\xi \cdot \cos(2\phi). \end{cases} \tag{B4}$$